biij

Image analysis in medical imaging: recent advances in selected examples

Dougherty G, PhD, FIET, SMIEEE

Applied Physics and Biomedical Imaging, California State University Channel Islands, California, United States of America

ABSTRACT

Medical imaging has developed into one of the most important fields within scientific imaging due to the rapid and continuing progress in computerised medical image visualisation and advances in analysis methods and computer-aided diagnosis. Several research applications are selected to illustrate the advances in image analysis algorithms and visualisation. Recent results, including previously unpublished data, are presented to illustrate the challenges and ongoing developments. © 2010 Biomedical Imaging and Intervention Journal. All rights reserved.

Keywords: Mammography; osteoporosis; tortuosity; scoliosis; osteoarthritis.

INTRODUCTION

A multitude of diagnostic medical imaging modalities are used to probe the human body. Interpretation of the resulting images requires sophisticated image processing methods that enhance visual interpretation, and image analysis methods that provide automated or semi-automated tissue detection, measurement and characterisation. In general, multiple transformations will be needed in order to extract the data of interest from an image, and a hierarchy in the processing steps will be evident, e.g. enhancement will precede restoration, which will precede analysis, feature extraction and classification. Often these are performed sequentially, but more sophisticated tasks will require feedback of parameters back to preceding steps so that the processing includes a number of iterative loops.

Several ongoing areas of research have been selected to highlight novel developments in analysis and display, in the hope that the methodologies may be transferred to other applications.

SELECTED APPLICATIONS

Mammography

Mammography is the single most important technique in the investigation of breast cancer, the most common malignancy in women. It can detect disease at an early stage when therapy or surgery is most effective. However, the interpretation of screening mammograms is a repetitive task involving subtle signs, and suffers from a high rate of false negatives (10%–30% [1, 2]), and false positives (10–20% [3, 4]). Computer-aided diagnosis (CAD) aims to increase the predictive value of the technique by pre-reading mammograms to indicate

* Corresponding author. Present address: Professor of Applied Physics and Medical Imaging, Bell Tower West, R. 2125, California State University Channel Islands, One University Drive, Camarillo, CA 93012, United States of America. Tel.: +805-437-8990; Fax: + 805-437-2765; E-mail: geoff.dougherty@csuci.edu (Geoff Dougherty).
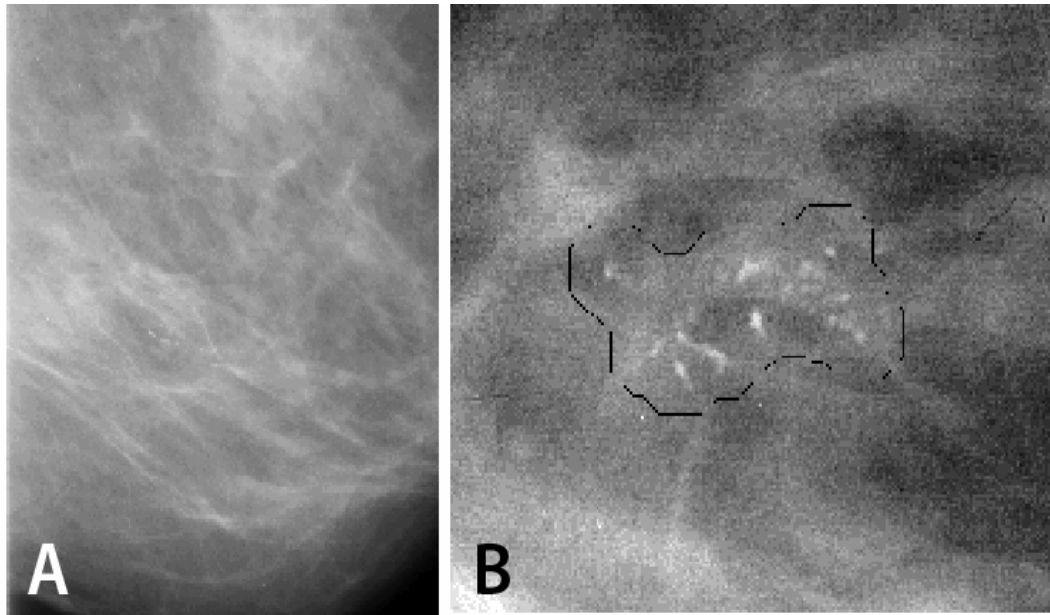
Figure 1 (a) A mammogram showing a cluster of microcalcifications and (b) computer-estimated margin around a cluster of microcalcifications.

the locations of suspicious abnormalities and analyse their characteristics, as an aid to the radiologist.

About 90% of breast cancers arise in the cells lining the milk ducts of the breast, and are known as *ductal carcinoma in situ* (DCIS). Once the tumour extends beyond the lining of the ducts it is termed invasive, and can metastasise to other sites in the body. Radiographic indications fall mainly into two categories, microcalcifications and lesions (masses) (Figure 1). Microcalcifications are the primary means of detecting *in situ* carcinomas (i.e. those within the milk ducts); they are typically in the order of several hundred microns or smaller in diameter, and tend to occur in clusters. Most lesions are ill-defined in shape, often with tissue strands or spiculations radiating out from them, and similar in radio-opacity to the surrounding normal tissue (Figure 2). The imaging requirements in mammography are stringent, both in terms of spatial and contrast resolution.
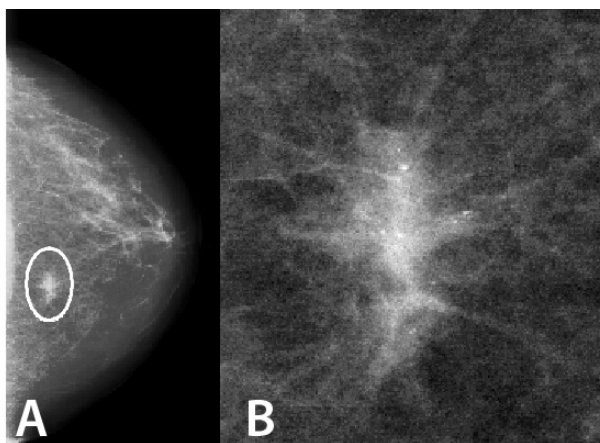

Figure 2 (a) A mammogram showing a stellate lesion and (b) a magnified image of the lesion.

CAD performance and reliability depends on a number of factors including the optimisation of lesion segmentation, feature selection, reference database size, computational efficiency, and the relationship between the clinical relevance and the visual similarity of the CAD results. Segmentation of the breast region serves to limit the search area for lesions and microcalcifications. It is also useful to adjust the grey values of the image to compensate for varying tissue thickness; one way to do this is to add grey values according to the *Euclidian distance map,* mapping distances to the skin line in a smoothed version of the mammogram [5]. Noise in the image can be reduced by median filtering, although this can disturb the shape and/or contrast of small structures. An improved technique [6] combines the results of morphological erosion and dilation using multiple structuring elements.

To improve the accuracy and reliability of mass region segmentation, a large number of computing algorithms have been proposed, developed and tested, including multi-layer topographic region growth algorithms [7, 8, 9], active contour (snake) modeling [10], adaptive region growth [11], a radial gradient index (RGI)-based modeling [12], and a dynamic programming-based boundary tracing (DPBT) algorithm [13]. Due to the diversity of breast masses and overlap of breast tissue in the 2-D projected images as well as the limited testing datasets, it is very difficult to compare the performance and robustness of these segmentation methods [14].

Features which are useful for characterising lesions include their degree of spiculation, shape and texture [15]. Spiculation features commonly involve the calculation of image gradient using, for example, the Sobel masks [16]. The cumulative edge gradient, from

the Sobel magnitude-of-edges image, can be plotted as a histogram of the radial angle, from the Sobel phase-of-edges image, to determine the degree of spiculation [17, 18]. The FWHM (full width at half maximum) of the gradient is able to distinguish spiculated masses from smooth masses. Others have used multi-scale oriented line detectors to detect and measure spiculated masses [19]. The centres of mass lesions tend to be circular so that specific filters can be used [20]. The boundary of the lesion can be unwrapped, and its difference from a smoothed version used to characterise the degree of spiculation [21]. Other relevant features include asymmetry, which would include automatic registration of left and right breast images [22], and changes with time [23]. Wavelets and Gabor filters have been extensively investigated and compared [24], and Gabor filters have performed better and corresponded well to the human vision (in particular for the sensitivity of edge detection) [25]. Other popular texture features derived from the co-occurrence matrices [26] and Fourier transformation [27] have also been tested. Recently, fractal dimension has been shown to be an effective and efficient metric for assessing texture in the detection and classification of suspicious breast mass regions [28]. Fractal dimension can be used to distinguish between malignant and benign breast masses [29], and has a high correlation with visual similarity [30, 31]. Since fractal dimension is a feature computed in the frequency domain, it has the advantage of being invariant to the lesion position and to rotation and scale. Most researchers extract several features and use principal component analysis to identify the most successful combinations. Different methods can be evaluated by receiver operating characteristic (ROC) analysis (Figure 3), but cannot be compared with each other unless the same image databases were used.
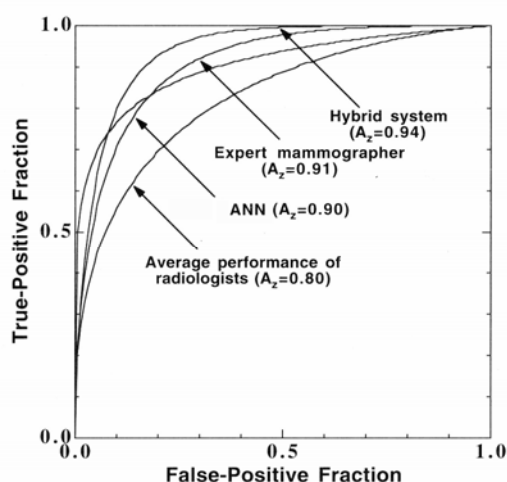

Figure 3 Receiver operating characteristic (ROC) curves illustrating the performances of a computer classification method and radiologists in the task of distinguishing between malignant and benign lesions. ANN indicates an artificial neural network using cumulative edge gradient features, and the hybrid system using several features. (Reprinted from [32], with permission from Elsevier).

Microcalcifications can be described by the morphology (shape, area, brightness *etc.*) of individual calcifications, and the spatial distribution and heterogeneity of individual calcifications within a cluster. They can be enhanced by thresholding the image, and morphologically opening it using a structuring element to eliminate very small objects while preserving the size and shape of the calcifications [33]. Isolated calcifications have little clinical significance, so many investigators have incorporated a clustering algorithm into the classification system, in which only clusters that contain more than a selected number of microcalcifications within a region of chosen size are retained [34]. Such schemes are easily implemented using the k-nearest-neighbour (k-NN) algorithm. Both spatial distribution and heterogeneity of the features within a cluster can be used to qualitatively correlate with a radiologist's criterion, and a classifier such as a neural network is used to estimate the likelihood of malignancy [35, 36]. Bayesian methods [37], discriminant analysis [38], rule-based methods [39] and genetic algorithms [40] have also been used in classification.

Computer assisted diagnosis (CAD) systems do not have to be perfect since they are used with a radiologist and not alone. Since the cost of a missed cancer is much greater than the misclassification of benign findings, they should be developed to reduce false negatives (*i.e.*, have a high sensitivity) even at the cost of some acceptable number of false positives (*i.e.*, reasonable specificity).

Bone strength and osteoporosis

Osteoporosis is a prevalent bone disease characterised by a loss of bone strength and consequent fracture risk. Because it tends to be asymptomatic until fractures occur, relatively few people are diagnosed in time for effective therapy to be administered. Clinically, bone mineral density, BMD, is widely used to diagnose and assess osteoporosis. Changes in bone mass are commonly used as a surrogate for fracture risk. Although bone mineral density, BMD, is widely used clinically, it has been increasingly realised that internal bone architecture is also an important determinant of the mechanical strength of bone and can lead to an earlier and more accurate diagnosis of osteoporosis [41–44]. Figure 4 shows how the loss of trabeculae in osteoporosis results in a less well-connected, and therefore weaker, structure. The limited resolution of commercial CT scanners precludes proper resolution of the trabecular structure; however, CT images retain some of this architectural information [45, 46], albeit degraded by the inadequate modulation transfer function (MTF) of the imaging system, and this can be characterised by the fractal signature of the trabecular bone (viz. its fractal dimension as a function of spatial frequency [47, 48] and its lacunarity [49], a measure of the distribution of gaps in an image).
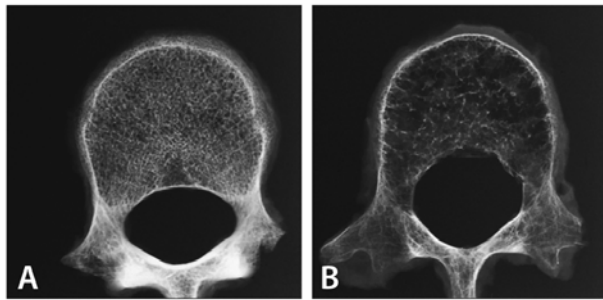
Figure 4 Radiographic images of lumbar vertebrae from (a) normal and (b) osteoporotic patients.

Fractal dimension describes how an object occupies space and is related to the complexity of its structure. Fractal dimension is related to the radial Fourier power spectrum of an image as a consequence of using fractional Brownian motion as a model for natural fractals. Estimates of the fractal signature, which are independent of the CT scanner used and its settings, can be obtained by correcting the power spectrum for image degradation due to noise, and for image blurring by the modulation transfer function (MTF) of the scanner [50]. However, changes in fractal dimension need to be interpreted with care. Global fractal dimension does not change monotonically with decalcification (Table 1).

Lacunarity measures the distribution of gap sizes in data: the greater the heterogeneity the greater the lacunarity. An efficient algorithm for estimating lacunarity analyses deviations from translational invariance of an image's brightness distribution using gliding-box sampling [49]. Lacunarity can be defined in terms of the local first and second moments, measured for each neighbourhood size, about every pixel in the image, i.e.

$$L(r) = 1 + \{ \text{var}(r) / \text{mean}^2(r) \}\} \qquad (1)$$

where mean(r) and var(r) are the mean and variance of the pixel values, respectively, for a neighbourhood size r. An average lacunarity value can be calculated across the scale range of the bone image to indicate the average gap (marrow) size and its degree of heterogeneity.

In a pilot study, we measured three features which have been used as surrogates for bone quality (bone mineral density, the average fractal dimension and the average lacunarity) from CT scans of sixteen patients whose bone strength had been previously assessed [51]. The data is shown in Table 2.

Table 1 A visual classification scheme for the assessment of the trabecular structure used for the determination of the degree of osteoporosis.

Class	Bone strength	Spongiosa pattern	Marrow size	Fractal dimension of ROI
1. Healthy	High	Homogeneously dense with granular structure	Small, homogeneous	Low, fractal
2. Beginning demineralisation	Normal	Discrete disseminated intertrabecular areas	Medium, inhomogeneous	High, multi-fractal
3. Osteopaenia	Low	Confluent intertrabecular areas less than 50% of the cross-sectional surface	Large, inhomogeneous	High, multi-fractal
4. Severe osteoporosis	Very low	Confluent intertrabecular areas more than 50% of the cross-sectional surface.	Very large, homogeneous	Low, multi-fractal

Table 2 Features measured from CT scans, and ground-truth class from bone strength.

Patient	BMD (mg cm^{-3})	Average fractal dimension	Average Lacunarity	Class
A	204	2.5	1.3	1
B	205	2.55	1.35	1
C	186.2	2.45	1.4	1
D	174.1	2.48	1.42	1
E	165.6	2.69	1.4	2
F	150.2	2.71	1.45	2
G	135.9	2.74	1.42	2
H	159.8	2.65	1.46	2
I	127.9	2.65	1.54	3
J	98.1	2.68	1.5	3
K	138.1	2.7	1.55	3
L	125.5	2.72	1.54	3
M	81.7	2.58	1.36	4
N	103.3	2.57	1.3	4
O	101.8	2.55	1.32	4
P	110.4	2.53	1.28	4

Linear discriminant analysis showed that the patients could be correctly classified into four classes (identified in table 1) according to bone strength on the basis of canonicals which are linear combinations of these three features (Figure 5), but misclassification rates of 12.5% occurred if only BMD and one other feature was used. These features, when used together, are potentially useful in monitoring bone strength and predicting future fracture risk using CT or MRI images.
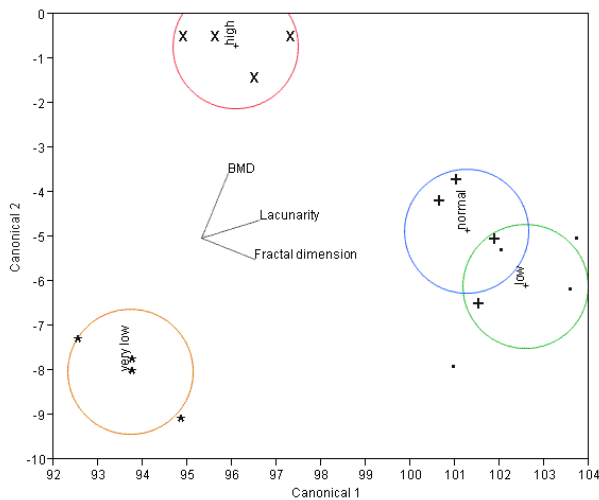

Figure 5 Canonical plot of surrogates for bone strength. Ground truth conditions are indicated by separate symbols. The directions of the three features are shown in the canonical space by the labelled rays. The size of each circle corresponds to a 95% confidence limit for the mean (marked with a +) of that group.

Tortuosity

The clinical recognition of elevated tortuosity or integrated curvature is important in the diagnosis of many diseases. Increased vascular tortuosity, for example, affects the flow haemodynamics and can lead to aneurysm (rupture of the blood vessels), and the tortuosity of retinal blood vessels can be an early indicator of systemic diseases.

Vessel tortuosity does not have a formal clinical definition but a tortuosity metric should be additive and invariant to affine transformations of a vessel (translation, rotation and scaling) [52–54] if it is to correlate with the qualitative assessment of an expert observer. One metric is the cumulative angle moved as an observer passed along the mid-line data points of the vessel, divided by the length of the vessel (which we shall refer to as M). Another metric is based on the root-mean-square curvature of a unit speed curve, obtained by an approximating polynomial spline fitting to the mid-line data points [55, 56]. The fitted curve is not required to pass through each point, but rather approach it to within a distance related to the radius of the local vessel, and is the smoothest path under these circumstances; it is not restricted to the discrete pixel grid so that it can more closely correspond to the actual vessel (Figure 6).

Approximating polynomial spline fitting captures the essential tortuosity of the vessels without having to place undue reliance on the accuracy of each extracted mid-line point, or employ arbitrary smoothing methods. Again this root-mean-square value would be divided by the length of the curve to give the tortuosity metric (which we shall refer to as K). Although these metrics are not strictly dimensionless, they are often referred to the length of the vessel in pixels and their units omitted: they can then be treated as numbers which rank the tortuosity of vessels obtained under the same imaging conditions.
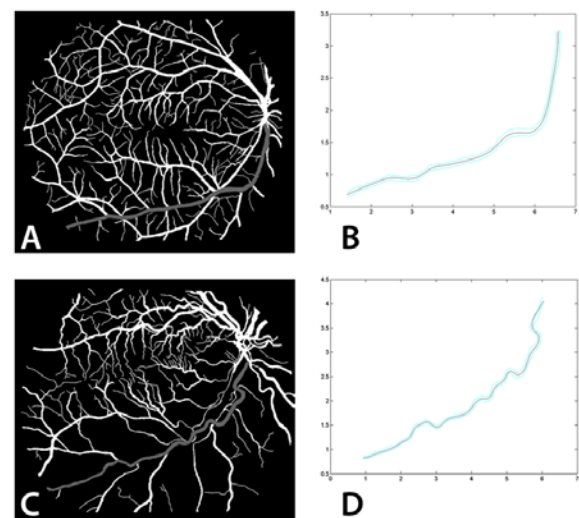

Figure 6 Binarised retinal image and the smoothest path through a selected vessel for a normal patient, (a) and (b), and a patient showing retinal pigmentosa, (c) and (d). (The axes in (b) and (d) are in relative units).

These analyses are construed directly in three dimensions (3-D) and their clinical validity has been established [57] using clinical data sets from computed tomography angiography, CTA, and magnetic resonance angiography, MRA.

These tortuosity metrics are able to distinguish between normal vessels and some retinal pathologies in retinal fundus images [58, 59], with a high positive predictive value, PPV (Table 3). Discriminant analysis shows that the two metrics can be used together for classifying vessels into the four classes based on their tortuosity (Figure 7). However, the misclassification rate is 21% using prior probabilities proportional to their occurrence. A more successful approach would be to use the tortuosity metrics together as a test for a single condition in referred patients already suspected of being at risk. Other features are relevant for particular pathologies, e.g. the number of aneurysms and extent of haemorrhaging and exudate in diabetic retinopathy [60, 61].

Table 3 Parameters characterising the tests for the three pathologies using the tortuosity metrics, *M* and *K*, whose values for the normals were 4.88 ± 1.17 and 7.74 ± 2.01, respectively. A of 330 vessels were measured. PPV (NPV) is the positive (negative) predictive value. Results are calculated using prevalences in the general population, and using the probabilities of each abnormal condition in the sample (viz. 7/19), in parentheses.

| Tortuosity metric		Retinitis pigmentosa	Diabetic retinopathy	Vasculitis
M	Mean ± sd	10.67 ± 1.10	6.69 ± 2.04	2.85 ± 0.50
	sensitivity	0.807 (0.993)	0.207 (0.520)	NA (0.917)
	specificity	1.000 (0.996)	0.999 (0.930)	NA (0.875)
	PPV	0.924 (0.993)	0.805 (0.812)	NA (0.811)
	NPV	1.000 (0.996)	0.978 (0.769)	NA (0.948)
K	Mean ± sd	17.62 ± 2.72	11.91 ± 2.22	4.99 ± 0.94
	sensitivity	0.705 (0.973)	0.263 (0.752)	NA (0.858)
	specificity	1.000 (0.990)	0.997 (0.907)	NA (0.809)
	PPV	0.924 (0.982)	0.733 (0.824)	NA (0.724)
	NPV	1.000 (0.984)	0.979 (0.862)	NA (0.907)
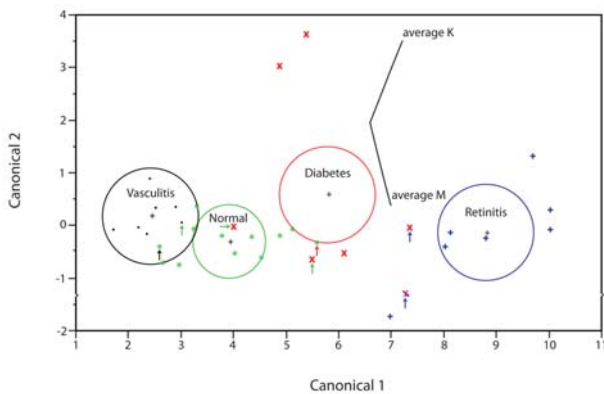
Figure 7 Canonical plot of data from 330 retinal vessels. Data from the ground truth conditions are indicated by separate symbols, each indicating the mean of 10 measurements. The directions of the features, M and K, are shown in the canonical space by the labeled rays. The size of each circle corresponds to a 95% confidence limit for the mean (marked with +) of that group; groups with significantly different values of tortuosity have non-intersecting circles. The small arrows indicate misclassified data points.

Scoliosis

Scoliosis is a complicated condition characterised by a lateral curvature of the spine and accompanied by rotation of the vertebrae on its axis [62]. Despite the risks associated with repeated exposure to ionising radiation

[63], radiography remains the most accurate method of assessing the scoliotic curvature. A scoliotic angle, determined from an erect antero-posterior (AP) radiograph of the full spine, is routinely used to clinically characterise the curvature. There are variations in the definition of the scoliotic angle and the methodology for measuring it [64]. Notwithstanding the differences, the methodologies identify the vertebrae at the upper and lower limits of the curve and, in some methods, the apical vertebrae (i.e. the most laterally deviated), and manually measure angles between defining points or lines within them.

Due to the errors associated with manual Cobb angle measurement from plain radiographs, a number of authors have developed computer-assisted techniques using digitised radiographs [65–69]. Several of these studies [65–67] report lower variability with computer-based techniques, but one [69] found no improvement in computer-based over manual measurement. However, all of these reported techniques require manual selection of features by the user, thus introducing inter and intra-observer measurement error. To the author's knowledge, no existing technique allows completely automated measurement of spinal curvature.

The tortuosity metrics (*M* and *K*) can be used to characterise the curvature of the spine in patients with idiopathic scoliosis by iteratively fitting piece-wise polynomial splines to the geometric centres of the vertebrae as seen in 2-D A-P radiographs [70]. The

Table 4 The correlation matrix, showing the (Pearson) correlation coefficients and their 95% confidence intervals

	Cobb	Ferguson	*M*	*K*
Cobb	1	0.994 [0.985,0.997]	0.862 [0.679, 0.944]	0.866 [0.730, 0.954]
Ferguson	0.994 [0.985,0.997]	1	0.850 [0.654, 0.939]	0.873 [0.702, 948]
M	0.862 [0.679, 0.944]	0.850 [0.654, 0.939]	1	0.996 [0.990, 0.998]
K	0.866 [0.730, 0.954]	0.873 [0.702, 948]	0.996 [0.990, 0.998]	1

values were strongly correlated with the Cobb and Ferguson scoliotic angles (Table 4). The tortuosity metrics use the positions of all the affected vertebrae, rather than just two or three select vertebrae, and produce a single measure of tortuosity for each patient even when a mixture of curvatures is present. The direct use of positional data removes the vagaries of defining end points and determining the appropriate lines to draw through variably-shaped endplates.

Since spinal curvature occurs in three-dimensions, it would be preferable to acquire three-dimensional images of the spine. It has been shown that reformatted coronal slices produced from transverse CT slices of supine patients and combined into a single image by a z-projection can be used to measure scoliotic angles [71]. The variability in angle measurements is similar, but the supine CT angles are smaller; a similar difference has been reported between standing and supine radiographs [72] because spinal geometry changes significantly between the two positions due to the effect of gravity. Supine CT curve measurements are valuable in biomechanical modeling of scoliosis to give a "zero load" configuration for the spine, which can be used as a starting point for numerical simulations.

Not only can the tortuosity metrics, *M* and *K*, deliver three-dimensional indices of scoliotic spine deformity, they can be used in a fully automated computer measurement system without the need for manual selection of points by the operator.

Osteoarthritis

Osteoarthritis (OA) is a progressive debilitating disease that results from degradation of the cartilage matrix that provides a low friction surface covering the ends of bones in joints [65]. Degraded cartilage is difficult to distinguish from healthy tissue with current imaging methods until degradation is well-advanced (Figure 8).
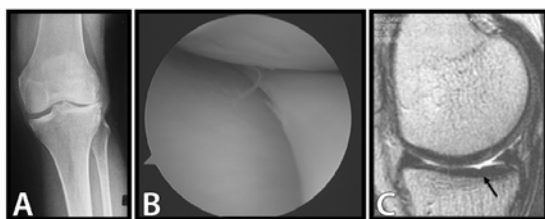
Figure 8 Images of a joint using (a) x-ray (b) arthroscopy and (c) MRI.

The initial stages of OA involve changes in water and proteoglycan content and in the orientation of the collagen fibre bundles in the surface of the cartilage (Figure 9). Recently it has been shown that the collagen fibres restrict the diffusion of water, which can be monitored using diffusion MRI [73].
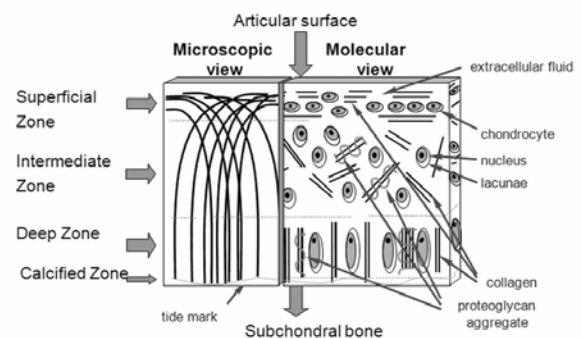
Figure 9 Cartilage microstructure.

Diffusion MRI, using a pair of de-phasing and re-phasing gradient pulses with a spin echo MRI sequence [74, 75], characterises these changes by using water diffusion properties as a probe. Diffusion MRI based on a tensor model of the diffusion anisotropy is known as diffusion tensor imaging (DTI). The diffusion tensor can be represented as an ellipsoid, defined by three eigenvectors and three eigenvalues (Figure 10).
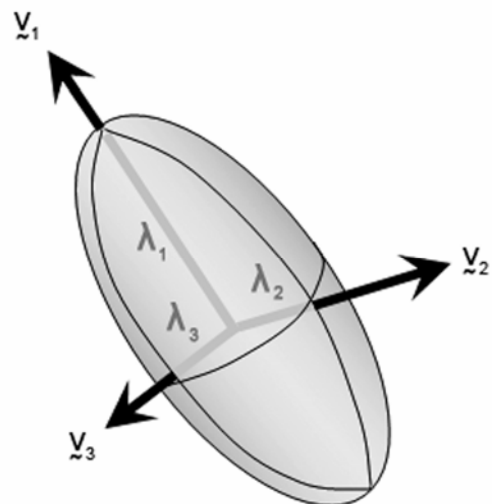
Figure 10 The diffusion ellipsoid is characterised by 3 eigenvectors, $\underline{v}_1, \underline{v}_2$ and $\underline{v}_3$, and 3 eigenvalues λ_1, λ_2 and λ_3.

The principal eigenvector (viz. the principal direction of diffusion) can be represented by a "quiver" plot, where each quiver represents the projection of the principal diffusion eigenvector on to the image plane (Figure 11). The autocorrelation function (ACF) of the quiver directions, in the articular surface and perpendicular to it, enables a determination of the sizes of the characteristic correlation distances.
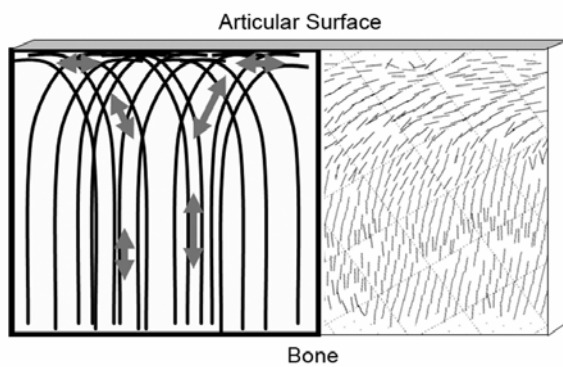
Figure 11 Orientation of collagen fibre bundles in normal cartilage in the form of 'arcades' shown schematically at left and a corresponding diffusion tensor image. The projections of the principal eigenvectors are shown as a quiver plot (at right). (After [76]).

Alternately the orientation of the principal eigenvector (with respect to the normal articular surface) can be mapped using a colour scale (Figure 12a), as can the maximum (or mean) diffusivity as determined by the principal eigenvalues (Figure 12b). The orientation angles from DTI correlate well with data from polarised light microscopy, PLM [76].
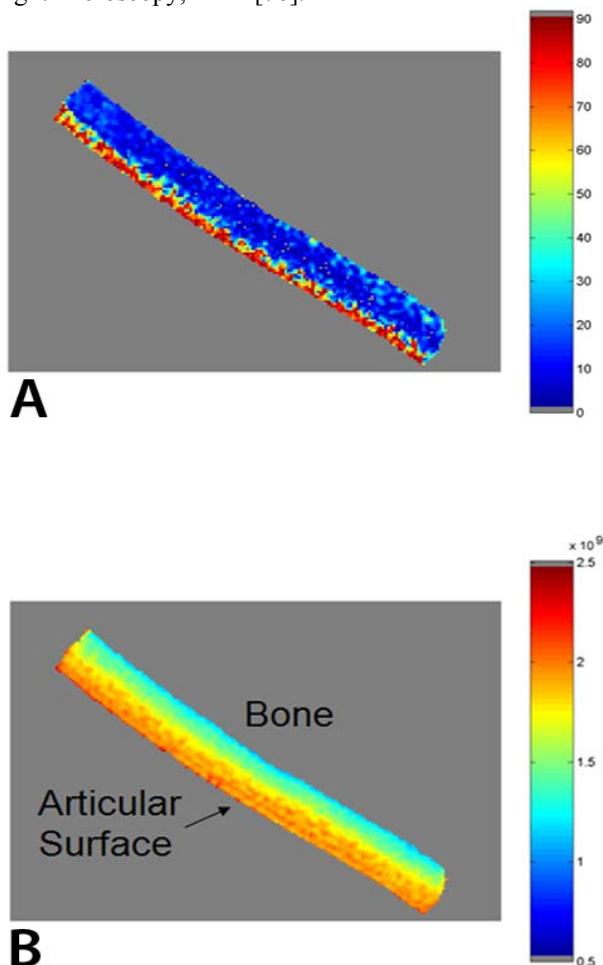

Figure 12 (a) Average orientation of principal eigenvector and (b) maximum diffusion eigenvalues (after [77]).

Experiments aimed at better understanding the mechanisms involved in cartilage degradation will continue. Early detection of these changes, when they may still be reversible, is key to the development of new approaches to treatment.

REFERENCES

1. Martin JE, Moskowitz M and Milbrath JR. Breast cancers missed by mammography. Am J Roentgen 1979; 132(5): 737–739.
2. Andersen SB, Vejborg I and von Euler-Chelpin M. Participation behaviour following a false positive test in the Copenhagen mammography screening programme. Acta Oncol 2008; 47(4): 550–555.
3. Kopans D. The positive predictive value of mammography. Am J Roentgen 1992; 158: 521–526.
4. Siegal EC, Angelakis EJ and Hartman A. Can peer review contribute to earlier detection of breast cancer? A quality initiative to learn from false-negative mammograms. Breast J 2008; 14(4): 330–334.
5. Bick U, Giger ML, Schmidt RA, Nishikawa RM and Doi K. Density correction of peripheral breast tissue on digital mammograms. Radiographics 1996; 16: 1403–1411.
6. Nishikawa RM, Giger ML, Doi K, Schmidt RA, Vyborny CJ, Ema T, Zhang W and Nagel RH. A noise reduction filter for use in a computerized scheme for the detection of clustered microcalcifications. Radiology 1993; 189P: 218.
7. Huo Z, Giger ML, Vyborny CJ, Bick U, Lu P, Wolverton DE and Schmidt RA. Analysis of spiculation in the computerized classification of mammographic masses. Med Phys 1995; 22(10): 1569–1579.
8. Zheng B, Chang YH and Gur D. Computerized detection of masses from digitized mammograms: comparison of single-image segmentation and bilateral-image subtraction. Acad Radiol 1995; 2(12): 1056–1061.
9. Eltonsy NH, Tourassi GD and Elmaghraby AS. A concentric morphology model for the detection omasses in mammography. IEEE Trans Med Imaging 2007; 26(6): 880–889.
10. Lobreqt S and Viergever MA. A discrete dynamic contour model. IEEE Trans Med Imag 1995; 14(1): 12–24.
11. te Brake GM and Karssemeijer N. Segmentation of suspicious densities in digital mammograms. Med Phys 2001; 28(2): 259–266.
12. Yuan Y, Giger ML, Li H, Suzuki K and Sennett C. A dual-stage method for lesion segmentation on digital mammograms. Med Phys 2007; 34(11): 4180–4193.
13. Dominguez AR and Nandi AK. Improved dynamic-programming-based algorithms for segmentation of masses in mammograms. Med Phys 2007; 34(11): 4265–4268.
14. Kupinski MA and Giger ML. Automated seeded lesions segmentation on digital mammograms. IEEE Trans Med Imag 1998; 17(4): 510–517.
15. Lladó X, Oliver A, Freixenet J, Marti R and Marti J. A textural approach for mass false positive reduction in mammography. Comput Med Imaging Graph 2009; 33(6): 415–422.
16. Dougherty G. Digital image processing for medical applications. Cambridge: Cambridge University Press, 2009.
17. Giger ML, Yin F-F, Doi K Metz CE, Schmidt RA and Vyborny CJ. Investigation of methods for the computerized detection and analysis of mammographic masses. Proc SPIE 1990; 1233: 183–184.
18. Huo Z, Giger ML, Vyborny CJ, Wolverton DE, Schmidt RA and Doi K. Automated computerized classification of malignant and benign masses on digitized mammograms. Acad Radiol 1998; 5(3): 155–168.
19. Parr T, Zwiggelaar R, Astley S, Boggis C and Taylor C. "Comparison of methods for combining evidence for speculated lesions", in *Digital Mammography*. The Netherlands: Kluwer Academic Publishers, 1998.
20. Kobatake, H. and Murakami, M. Adaptive filter to detect rounded convex regions: Iris filter. Proc Int Conf Pattern Recognition 1996; 2: 340–344.
21. Giger ML, Vyborny CJ and Schmidt, RA. Computerized

characterization of mammographic masses: analysis of spiculations. Cancer Letters 1994; 77(2-3): 201–211.

22. Yin FF, Giger ML, Doi K, Vyborny CJ and Schmidt RA. Computerized detection of masses in digital mammograms: automated alignment of breast images and its effect on bilateral-subtraction technique. Med Phys 1994; 21(3): 445–452.

23. Sallam M and Bowyer K. "Detecting abnormal densities in mammograms by comparison to previous screening", in *Digital Mammography '96*, 417–20, Elsevier, 1996.

24. Ortega M, Rui Y, Chakrabarti K, Porkaew K, Mehrotra S and Huang TS. Supporting ranked Boolean similarity queries in MARS. IEEE Trans Knowledge Data Eng 1998; 10(6): 905–925.

25. Daugman JG. High confidence visual recognition of persons by a test of statistical independence. IEEE Trans Pattern Anal Machine Intel 1993; 15(11): 1148–1161.

26. Kuo WJ, Chang RF, Lee CC, Moon WK and Chen DR. Retrieval technique for the diagnosis of solid breast tumors on sonogram. Ultrasound Med Biol 2002; 28(7): 903–909.

27. Milanese R and Cherbuliez M. A rotation, translation and scale-invariant approach to content-based image retrieval. J Visual Commun Image Represent 1999; 10(2): 186–196.

28. Park SC, Wang X and Zheng B. Assessment of performance improvement in content-based medical image retrieval schemes using fractal dimension. Acad Radiol 2009; 16(10): 1171–1178

29. Velanovich V. Fractal analysis of mammographic lesions: a feasibility study quantifying the difference between benign and malignant masses. Am J Med Sci 1996; 311(5): 211–214.

30. Chevallet JP, Maillot N and Lim JH. Concept Propagation Based on Visual Similarity Application to Medical Image Annotation. Proc Third Asia Information Retrieval Symposium. 2006; 4182: 514–521.

31. Soares F, Andruszkiewicz P, Freire M, Cruz P, Pereira M, Siemens SA and Perafita. Self-Similarity Analysis Applied to 2D Breast Cancer Imaging. Proc International Conf Systems and Networks Communications 2007; 1: 1–6.

32. Huo Z, Giger ML, Vyborny CJ, Wolverton DE, Schmidt RA and Doi K. Automated computerized classification of malignant and benign mass lesions on digitized mammograms. Academic Radiology 1998; 5(3): 155–168.

33. Dougherty, G. Computerized evaluation of mammographic image quality using phantom images. Comp Med Imaging and Graphics 1998; 22(5): 365–373.

34. Nishikawa RM, Giger ML, Doi K, Vyborny CJ and Schmidt RA. Computer-aided detection of clustered microcalcifications: an improved method for grouping detected signals. Med Phys 1993; 20(6): 1661–1666.

35. Jiang Y, Nishikawa RM, Schmidt RA, Metz CE, Giger ML and Doi K. Improving breast cancer diagnosis with computer-aided diagnosis. Acad Radiol 1999; 6(1): 22–33.

36. Sun X, Qian W and Song D. Ipsilateral-mammogram computer-aided detection of breast cancer. Comp Medical Imaging and Graphics 2004; 28(3): 151–158.

37. Bankman IN, Christens-Barry, WA, Kim DW, Weinberg IN, Gatewood OB and Brody WR Automated recognition of microcalcification clusters in mammograms. Proc SPIE 1993; 1905: 731–738.

38. Swets JA, Getty DJ, Pickett RM, D'Orsi CJ, Seltzer SE and McNeil BJ. Enhancing and evaluating diagnostic accuracy. Med Decis Making 1991; 11(1): 9–18

39. Chang YH, Zheng B, Good WF and Gur D. Identification of clustered microcalcifications on digitized mammograms using morphology and topography-based computer-aided detection schemes: a preliminary experiment. Invest Radiol 1998; 33(10): 746–751.

40. Zheng B, Chang YH, Wang XH, Good WF and Gur D. Feature selection for computerized mass detection in digitized mammograms by using a genetic algorithm. Acad Radiol 1999; 6(6): 327–332.

41. Goldstein SA, Goulet R and McCubbrey D. Measurement and significance of three-dimensional architecture to the mechanical integrity of bone. Calcif Tissue Int 1993; 53(Suppl 1): S127–S133.

42. Fazzalari NL and Parkinson IH. Fractal dimension and architecture of trabecular bone. J Path 1996; 178(1): 100–105.

43. Jiang C, Pitt RE, Bertram JE and Aneshansley DJ. Fractal-based image texture analysis of trabecular bone architecture. Med Biol Eng Comput 1999; 37(4): 413–418.

44. Kraus VB, Feng S, Wang S, White S, Ainslie M, Brett A, Holmes A and Charles HC. Trabecular morphometry by fractal signature analysis is a novel marker of osteoarthritis progression. Arthritis Rheum 2009; 60(12): 3711–3722.

45. Dougherty G. A comparison of the texture of computed tomography and projection radiography images of vertebral trabecular bone using fractal signature and lacunarity. Med Eng Phys 2001; 23(5): 313–321.

46. Hua Y, Nackaerts O, Duyck J, Maes F and Jacobs R. Bone quality assessment based on cone beam computed tomography imaging. Clin Oral Implants Res 2009; 20(8): 767–771.

47. Dougherty G and Henebry GM. Fractal signature and lacunarity in the measurement of the texture of trabecular bone in clinical CT images. Med Eng Phys 2001; 23(6): 369–380.

48. Zaia A, Eleonori R, Maponi P, Rossi R and Murri R. MR imaging and osteoporosis: fractal lacunarity analysis of trabecular bone. IEEE Trans Inf Technol Biomed 2006; 10(3): 484–489.

49. Plotnick RE, Gardner RH and O'Neill RV. Lacunarity indices as measures of landscape texture. Landscape Ecology 1993; 8(3): 201–211.

50. Dougherty G and Henebry, GM. Lacunarity analysis of spatial pattern in CT images of vertebral trabecular bone for assessing osteoporosis. Med Eng Phy. 2002; 24(2): 129–138.

51. Keaveny TM. Biomechanical computed tomography-noninvasive bone strength analysis using clinical computed tomography scans. Ann N Y Acad Sci 2010 ; 1192(1): 57–65.

52. Hart WE, Goldbaum M, Côté B, Kube P and Nelson MR. Measurements and classification of retinal vascular tortuosity. Int J Med Inform 1999; 53(2-3): 239–252.

53. Saidlear CA. Implementation of a quantitative index for 3D arterial tortuosity. MSc Thesis. University of Dublin; 2002.

54. Bullitt E, Gerig G, Pizer SM, Lin W and Aylward SR. Measuring tortuosity of the intracerebral vasculature from MRA images. IEEE Trans Med Imag 2003; 22(9): 1163–1171.

55. Kersey SN. On the problems of smoothing and near interpolation. Math Comput 2003; 72(244): 1873–85.

56. Johnson MK and Dougherty G. Robust measures of three-dimensional vascular tortuosity based on the minimum curvature of approximating polynomial spline fits to the vessel mid-line. Med Eng Phys 2007; 29(6): 677–690

57. Dougherty G and Johnson MK. Clinical validation of three-dimensional tortuosity metrics based on the minimum curvature of approximating polynomial splines. Med Eng Phys 2008; 30(2): 190–198.

58. Dougherty G and Johnson MK. Clinical applications of three-dimensional tortuosity metrics. Proc SPIE 2007; 6511: 1–9.

59. Dougherty G, Johnson MK and Wiers MD. Measurement of retinal vascular tortuosity and its application to retinal pathologies. Med Biol Eng Comput 2010; 48(1): 87–95.

60. Fleming AD, Philip S, Goatman KA, Olson JA and Sharp PF. Automated microaneurysm detection using local contrast normalization and local vessel detection. IEEE Trans Medical Imag 2006; 25(9): 1223–1232.

61. Jelinek HJ, Cree MJ, Worsley D, Luckie A and Nixon P. An automated microaneurysm detector as a tool for identification of diabetic retinopathy in rural optometric practice. Clin Expt Optometry 2006; 89(5): 299–305.

62. Krawczynski A, Kotwicki T, Szulc A and Samborski W. Clinical and radiological assessment of vertebral rotation in idiopathic scoliosis. Ortop Traumatol Rehabil 2006; 8(6): 602–607.

63. Nash CL Jr, Gregg EC, Brown RH and Pillai K. Risks of exposure to x-rays in patients undergoing long-term treatment for scoliosis. J Bone Joint Surg Am 1979; 61(3): 371–374.

64. Diab KM, Sevastik JA, Hedlund R and Suliman IA. Accuracy and applicability of measurement of the scoliotic angle at the frontal plane by Cobb's method, by Ferguson's method and by a new method. Eur Spine J 1195; 4(5): 291–295.

65. Cheung J, Wever DJ, Veldhuizen AG, Klein JP, Verdonck B, Nijlunsing R, Cool JC and Van Horn JR. The reliability of quantitative analysis on digital images of the scoliotic spine. Eur Spine J 2002; 11(6): 535–542.

66. Shea KG, Stevens PM, Nelson M, Smith JT, Masters KS and Yandow S. A comparison of manual versus compter-assisted radiographic measurement: intraobserver measurement variability for Cobb angles. Spine 1998; 23(5): 551–555.

67. Chockalingam N, Dangerfield PH, Giakas G, Cochrane T and

Dorgan JC. Computer-assisted Cobb measurement of scoliosis. Eur Spine J 2002; 11(4): 353–357.

68. Dutton KE, Jones TJ, Slinger BS, Scull ER and O'Connor J. Reliability of the Cobb angle index derived by traditional and computer-assisted methods. Aust Phys Eng Sci Med 1989; 12(1): 16–23.

69. Zmurko MG, Mooney JF 3rd, Podeszwa DA, Minster GJ, Mendelow MJ and Guirgues A. Inter- and intraobserver variance of Cobb angle measurements with digital radiographs. J Surg Orthopaedic Advances 2003; 12(4): 208–13.

70. Dougherty G and Johnson MK. Assessment of scoliosis by direct measurement of the curvature of the spine. Proc SPIE 2009; 72603Q: 1–10.

71. Adam CJ, Izatt MT, Harvey JR and Askin GN. Variability in Cobb angle measurements using reformatted computerized tomography scans. Spine 2005; 30(14): 1664–1669.

72. Torell G, Nachemson A, Haderspeck-Grib K and Schultz A. Standing and supine Cobb measures in girls with idiopathic scoliosis. Spine 1985; 10(5): 425–427.

73. Meder R, de Visser SK, Bowden JC, Bostrom T and Pope JM. Diffusion tensor imaging of articular cartilage as a measure of tissue microstructure. Osteoarthritis Cartilage 2006; 14(9): 875–881.

74. Stejskal E and Tanner J. Spin diffusion measurements: spin echoes in presence of a time-dependent field gradient. J Chem Phys 1965; 42(1): 288–292.

75. Hagmann P, Jonasson L, Maeder P, Thiran JP, Wedeen VJ and Meuli R. Understanding diffusion MR imaging techniques: from scalar diffusion-weighted imaging to diffusion tensor imaging and beyond. Radiographics 2006; 26(Suppl 1): S205–23.

76. Pope JM, de Visser SK, Wellard RM and Momot KI. MR Micro-imaging of Articular Cartilage. 10th Int Conf on MR Microscopy, Montana, USA, 2009 Aug. 30 - Sept. 4.

77. de Visser SK, Bowden JC, Wentrup-Byrne E, Rintoul L, Bostrom T, Pope JM and Momot KI. Anisotropy of collagen fibre alignment in bovine cartilage: comparison of polarised light microscopy and spatially resolved diffusion-tensor measurements. Osteoarthritis Cartilage 2008; 16(6): 689–697.